Experimental evaluation of Marangoni stress and surfactant concentration at interface of contaminated single spherical drop using spatiotemporal filter velocimetry

Hosokawa, Shigeo
Masukura, Yuya
Hayashi, Kosuke
Tomiyama, Akio

(Citation)
International Journal of Multiphase Flow,97:157-167

(Issue Date)
2017-12

(Resource Type)
journal article

(Version)
Accepted Manuscript

(URL)
https://hdl.handle.net/20.500.14094/90004649

Experimental Evaluation of Marangoni Stress and Surfactant Concentration at Interface of Contaminated Single Spherical Drop Using Spatiotemporal Filter Velocimetry

Shigeo Hosokawa[*,**], Yuya Masukura[*], Kosuke Hayashi[*,**], Akio Tomiyama[*,**]

* *Department of Mechanical Engineering,*
Graduate School of Engineering,
Kobe University
** *Complex Fluid and Thermal Engineering Research Center,*
Kobe University
1-1 Rokkodai, Nada, Kobe, Hyogo 657-8501, Japan,
Phone and Fax: +81-78-803-6132
E-mail: hosokawa@mech.kobe-u.ac.jp

Abstract Spatiotemporal filter velocimetry (SFV) was extended to Lagrangian measurements with boundary-fitted measurement areas, and was applied to flows about single spherical drops of glycerol-water solution falling in stagnant silicon oil under clean and contaminated conditions to examine its applicability to the estimation of the Marangoni stress and surfactant concentration at a moving interface. Effects of bulk concentration of surfactant on the velocity field, the Marangoni stress and the surface concentration of surfactant were discussed from the measured data. As a result, we confirmed that accurate velocity distribution in the vicinity of the interface measured by SFV enables us to evaluate interfacial velocity and interfacial shear stresses and to estimate the Marangoni stress, interfacial tension and surfactant concentration at the interface with the assumption of negligible surface viscosity. The flow inside the drop and the interfacial velocity become weak due to the Marangoni stress caused by the gradient of surfactant concentration at the interface as the bulk concentration of surfactant increases. These results demonstrate that SFV is of great use in experimental analysis of adsorption and desorption kinetics at a moving interface.

Keywords: Drop, Marangoni effect, Spatiotemporal filter velocimetry, Surfactant, Interface

Highlights

- Spatiotemporal filter velocimetry is extended to boundary–fitted measurement regions (BF-SFV).
- BF-SFV enables us to measure velocity distribution in the vicinity of an interface accurately.
- Interfacial velocity and interfacial shear stress can be evaluated from the measured velocity distribution.
- Distributions of the Marangoni stress, interfacial tension and surfactant concentration at the interface are successfully estimated from the accurate velocity distributions.

1. Introduction

Adsorption of surfactants at an interface changes the interfacial tension and induces the gradient of the interfacial tension, i.e., the Marangoni stress which affects the boundary condition at the interface and alters rates of mass and momentum transfer between the two fluids. Thus, knowledge on adsorption-desorption kinetics at an interface is of fundamental importance to understand motion and mass transfer of drops and bubbles. Many studies (Levich, 1962; Borwankar and Wasan, 1983; Bleys and Joos, 1985) have been carried out for understanding and modeling adsorption-desorption kinetics. Most of them have dealt with a static interface in a quiescent system. Several numerical simulations (Cuenot et al., 1997; Takagi et al., 2003; Hayashi and Tomiyama, 2012) have been conducted by using an adsorption-desorption model for the quiescent system to predict distributions of surfactant concentration and the Marangoni stress at the moving interface of a bubble or a drop. However, the applicability of the model to a moving interface has not been examined through comparisons with experimental data due to the difficulty in measuring surfactant concentration and the Marangoni stress at a moving interface. Hence, development of an experimental evaluation method of the Marangoni stress and surfactant concentration at a moving interface is required for validations of numerical simulation and models used in those simulations.

The Marangoni stress acting on an interface balances with the inner and outer viscous shear stresses at the interface, in other words, a jump in the interfacial shear stress takes place at the interface when the Marangoni stress occurs. Hence, an accurate measurement of interfacial shear stresses in both phases would enable us to evaluate the Marangoni stress. Imaging velocimetry such as PIV and spatiotemporal filter velocimetry (SFV; Hosokawa and Tomiyama 2012; Hosokawa et al., 2013) may provide velocity distributions in the vicinity of an interface. However, the presence of an interface in a measurement region decreases the measurement accuracy. Oguma and Fujisawa (2007) proposed PIV in a boundary-fitted measurement region in which the recorded particle image was transformed into a rectangular shape to calculate cross-correlation of the images. The boundary-fitted measurement region enables us to accurately evaluate the gradient of tangential velocity at an interface, compared with rectangular measurement regions. PIV, however, measures the translation velocity of multiple particles in an

interrogation area, so that measured velocity is an area-averaged velocity and the minimum size of the interrogation area (spatial resolution) strongly depends on particle concentration. The transformation of digital particle images in the boundary-fitted region induces expansion or compression of a pixel size, i.e., particle size, and therefore, the particle size in the transformed image is not uniform and depends on the particle position. This position-depending particle-size distribution could be an error source and the error becomes large as the curvature or deformation of the boundary/interface becomes large. Since SFV measures velocity of a single particle in a fixed measurement region and does not use a spatial correlation process, it might be easily extended to an arbitrary measurement region fitted to an interface without transformation of particle images. Since accuracy of velocity measurement and spatial and temporal resolutions of SFV are as high as laser Doppler velocimetry (LDV) (Hosokawa and Tomiyama, 2012), extension of SFV to boundary fitted measurement region may be a promising way to accurate measurement of interfacial shear stress and the Marangoni stress at an interface.

For surfactant concentration at an interface, several measurement methods have been proposed so far. Radiotracer (Dixon, 1949; Tajima et al., 1970), X-ray absorption (Takiue et al., 2003) and neutron reflection methods (Manning-Benson et al., 1998) can measure surfactant concentration at an interface and are successful tools to understand surface concentration and surface structure at an equilibrium state. Their spatial and temporal resolutions are, however, not high enough to capture adsorption-desorption kinetics at a moving interface. Optical methods (Shen, 1989; Bain, 1998), i.e., ellipsometry, second harmonic generation (SHG) and sum-frequency generation (SFG) provide better spatial resolutions, and therefore, they are applied to distribution measurement of surface concentration at a moving interface in a static shape (Manning-Benson et al., 1997, Hutchison et al., 1999; Vogel et al., 2001). However, the optical signal deeply depends on types of surfactant, and therefore, measurements are valid only for specific surfactants and calibration is necessary for each surfactant. A fluorescently tagged surfactant lipid (Bull et al., 1999) have been used to measure surfactant distribution at an interface (Fallest et al., 2010; Strickland et al., 2015) and provided spatial and temporal distributions of surface concentration of the surfactant. However, it is not easy to carry out the measurement for various surfactants having various adsorption and desorption constants. Since the gradient of surface concentration of surfactant

induces the gradient of interfacial tension, i.e, the Marangoni stress, the surface concentration could be evaluated from the Marangoni stress.

In this study, the SFV is extended to Lagrangian measurement with boundary-fitted measurement regions, and it is applied to flows about single drops of glycerol-water solution falling in a stagnant silicone oil under clean and contaminated conditions to demonstrate the applicability of SFV to velocity measurements in the vicinity of the interface. Velocity distributions not only outside but also inside the drops are measured by using a refractive index matching method. The interfacial velocity and interface shear stress are evaluated from the measured velocity distribution near the interface. The Marangoni stress, interfacial tension and concentration of surfactants at an interface are estimated from the measured velocity distributions to examine the availability of SFV for validation of numerical simulation taking into account adsorption and desorption of surfactants at an interface.

2. Measurement Method

2.1 Principle of Spatiotemporal filter velocimetry

Figure 1 shows the principle of SFV, which processes time-series particle images recorded by a high-speed camera in the image acquisition step. A spatiotemporal filter $F_{SF}(x,y,t)$, which is a cyclic function in space, is multiplied to an intensity distribution $I(x,y,t)$ of an image in an interrogation area, and the resultant intensity distribution is integrated in the interrogation area to obtain the integral intensity $I_{SF}(x_c, y_c, t)$ (spatiotemporal filtering step):

$$I_{SF}(x_c, y_c, t) = \int_{y_c-\frac{\Delta y}{2}}^{y_c+\frac{\Delta y}{2}} \int_{x_c-\frac{\Delta x}{2}}^{x_c+\frac{\Delta x}{2}} I(x, y, t) F_{SF}(x, y, t) dx dy \qquad (1)$$

where t is the time, (x_c, y_c) the center position of the interrogation area, and Δx and Δy are the sizes of the area in x and y directions, respectively. When $F_{SF}(x, y, t)$ is a periodic function (period L_x) with respect to x (ex. $\cos(2\pi x/L_x)$) and a particle with velocity v_x moves in the area, $I_{SF}(x_c, y_c, t)$ periodically fluctuates with the frequency v_x/L_x. Hence, the frequency estimation of I_{SF} yields particle velocity

(frequency/velocity evaluation step). The perpendicular velocity component v_y can be measured by using a cyclic function with respect to y as F_{SF}. Thus, we can evaluate two velocity components of each particle in an arbitrary interrogation area in the imaging plane from the time-series particle images. The direction of velocity can be determined by using a moving filter function like the frequency shift in LDV measurements. In this study, we use a cosine function for F_{SF}, and a wavelet analysis is adopted to evaluate the frequency of I_{SF}. Details of SFV can be found in Hosokawa and Tomiyama (2012).

2.2 Extension of SFV to boundary-fitted interrogation area

In SFV measurements of flow containing interfaces or curved walls, the interface or the wall surface passes through an interrogation area is apt to cause measurement errors. Hence, the measurement accuracy and resolution in the vicinity of an interface or surface tend to be lower than those away from the interface/boundary in spite of the importance of the flow near the interface/wall. SFV is, therefore, extended to a general curvilinear coordinate as shown in Fig. 2. Interrogation areas are formed to fit the interface/boundary, and therefore, the areas are not rectangle but arbitrary shaped. The spatiotemporal filter F_{SF} in the curvilinear coordinate (ξ, η), is projected onto the non-rectangular interrogation area to obtain I_{SF}:

$$I_{SF}(x_c, y_c, t) = \iint I(x, y, t) M(x, y, t) F_{SF}(\xi(x, y, t), \eta(x, y, t), t) dx dy \quad (2)$$

where M is the window function which takes 1 and 0 in the inside and the outside of the interrogation area, respectively. The area of the integration is an arbitrary region which contains the interrogation area. The velocity in the (ξ, η) plane can be evaluated from the frequency of fluctuating I_{SF}.

3. Experimental Apparatus

SFV was applied to flows about single drops of glycerol-water solution (53.5 wt%, viscosity: $\mu_D = 6.13$ mPa s, density: $\rho_D = 1132$ kg/m^3) falling in stagnant silicone oil (Shinetsu Silicone, KF-96-300cs; viscosity: $\mu_C = 299$ mPa s, density:

ρ_C = 967 kg/m^3) in a rectangular container (170(W) x 170(D) x 500(H) mm) under clean and contaminated conditions. Figure 3 shows the schematic of the experimental apparatus. Millipore water was used to prepare the glycerol-water solution. The concentration of the glycerol-water solution was determined so as to match the refractive index of the solution with that of the silicone oil (Ninomiya and Yasuda, 2006). The experimental conditions are summarized in Table 1. Triton X-100 was solved in the glycerol-water solution as surfactant. The surfactant concentrations C were 0.0, 0.2, 0.5, 1.0 and 10 x 10^{-2} mol/m^3 for Cases 1, 2, 3, 4 and 5, respectively. The drop size was constant (8.3 mm) in all the cases, and the drop Reynolds number was less than unity. The drop was released from the nozzle located at the center of the cross-section of the container just below the surface of the silicone oil. The duration from the start of drop generation to the release of the drop was kept constant (1 sec.) so as to keep the initial contamination level constant. The temperatures of the fluids were fixed at 25 $\pm$ 0.5 ^{o}C.

Silicon dioxide particles (mean diameter: 3 μm) were added to both fluids as tracer particles. The particles mixed with ethanol and mixed well to elute oil-based contaminants. Then, they were extracted from the contaminated ethanol by a centrifugal separation. Then, the particles were mixed and stirred well with Millipore water to remove ethanol and water-based contaminants. The particles were extracted by the centrifugal separation. These processes were repeated at least three times and the resultant particles were dried and added to the liquid phases. Rhodamine B was dissolved in the glycerol-water solution at the concentration of 5.0x10^{-3} mol/m^3 to distinguish the drop region from the other in visualized images. The vertical center plane of the drop was visualized by a laser sheet (thickness: 0.2 mm, width: 25 mm, wavelength: 532 nm) irradiated from the bottom of the container. The particle images were recorded by a high-speed camera (Photron, FASTCAM SA-X2, frame rate: 12500 fps, resolution: 0.02 mm/pixel) and the velocity distributions were measured by SFV. The velocity measurements were carried out at y = 250 $\pm$ 10 mm below the nozzle tip. The drop reached a quasi-terminal condition before it reached y = 150 mm. The second camera located perpendicular to the high-speed camera was used to check whether the laser sheet passed through the center plane of the drop. Since the drop is spherical in the present conditions, cylindrical coordinates, the origin of which was the center of drop, was used to measure velocity in the vicinity of the interface. The size of the interrogation

region was 0.3 mm in the radial direction and 6 deg. in tangential direction. Velocity in the regions far from the interface was measure by using a rectangular area (0.3 x 0.3 mm). The uncertainty in SFV measurement was confirmed to be less than 5 % in our previous study (Hosokawa and Tomiyama, 2012).

4. Results and Discussion

4.1 Validation of measured velocity

Figure 4 shows the pathlines of tracer particles, the distributions of velocity $\boldsymbol{v}$ measured by SFV and the streamlines calculated from the measured velocity distributions for the clean and contaminated systems. x and y are the coordinates whose origin was fixed at the center of drop. The distance from the drop center and the velocity $\boldsymbol{v}$ are normalized by the drop radius R and the terminal velocity V_T, respectively. Internal circulation was successfully measured in the clean system (Case 1), and it becomes weaker as the surfactant concentration increases. The velocity inside the drop in Case 5 almost vanishes, and therefore, the velocity around the drop clearly decreases due to the immobile interface. As a result, the terminal velocity of the drop agrees well with the Stokes solution for a spherical solid particle. Hence, this condition can be regarded as the fully contaminated system. In the medium contamination cases (Cases 2, 3 and 4), the internal circulation is not fore-aft symmetric. This implies that the interface is clean in the front region and contaminated in the rear region. As C increases, the stagnant cap formed in the tail region becomes larger, and the internal circulation moves forward and weakens. This attenuation of the internal circulation changes the boundary condition at the interface and increases the drag acting on the drop. As a result, the terminal velocity of the drop decreases with increasing C as shown in Table 1.

Figure 5 shows comparisons between the measured and theoretical tangential velocity distributions in the clean and contaminated drops. The curves are the following Hadamard-Rybczynski and Stokes solutions for a clean drop and a solid sphere, respectively.

$$v_\theta = \begin{cases} \frac{V_T \sin\theta}{2r}\left[2r - \frac{R(2+3\kappa)}{2(1+\kappa)} - \frac{\kappa R^3}{2r^2(1+\kappa)}\right] & \frac{r}{R} \geq 1 \\ -\frac{V_T \sin\theta}{2(1+\kappa)}\left[1 - \frac{2r^2}{R^2}\right] & \frac{r}{R} < 1 \end{cases} \quad \text{for a clean drop} \quad (3)$$

$$v_\theta = \begin{cases} \frac{V_T \sin\theta}{2r}\left[2r - \frac{3R}{2} - \frac{R^3}{2r^2}\right] & \frac{r}{R} \geq 1 \\ 0 & \frac{r}{R} < 1 \end{cases} \qquad \text{for a solid sphere (4)}$$

where θ is the angle from the nose of the drop and κ the viscosity ratio μ_D/μ_C. The measured velocity distributions about the clean and contaminated drops agree well with the theories, which indicates that SFV accurately measured velocity distributions about the drops. It is also confirmed that the velocity distribution about the fully contaminated drop is almost the same as that about a solid sphere (Clift et al., 1978).

Figure 6 shows the azimuthal distribution of the tangential component $v_{\theta int}$ of the velocity at the interface, which is evaluated by extrapolating the interfacial velocities from inside and outside velocity distributions in the vicinity of the interface and taking the average of the interfacial velocities. The distributions in Cases 1 and 5 agree well with the Hadamard-Rybczynski and Stokes solutions (Eqs. (3) and (4) at $r = R$), respectively. The small deference between the measured and theoretical values in the rear part of the clean drop (Case 1, θ > 150 deg.) might be due to slight contamination in the clean system. In Case 2, the velocity distribution in the front part of the drop agrees with that of the clean drop (θ < 60 deg.). This region becomes small with increasing *C*, i.e., θ < 30 and 10 for Cases 3 and 4, respectively. The velocity in Case 2 in the rear part (θ > 150 deg.) is almost the same as that of the fully-contaminated drop, i.e., zero. The angle θ at which the velocity reaches the value of the fully-contaminated system becomes small as *C* increases, i.e, θ = 120 and 90 deg. for Cases 3 and 4, respectively. These velocity distributions in the intermediate surfactant concentrations disagree with Levich's assumption (1962), i.e., the sinusoidal distribution, used to deduce the terminal velocity of a fluid particle in a contaminated system.

Figure 7 (a) shows the radial component of the gradient of the tangential velocity at the interface, which was evaluated from the inner and outer velocity distributions. The measured velocity gradients agree well with theoretical gradients calculated from Eqs. (3) and (4) in clean and fully-contaminated systems, respectively. However, there is a large gradient region in the outside of the drop and a negative velocity gradient in the inside around θ = 140 deg. in Case 2. The

interfacial velocity in $0 < \theta < 90$ deg. in Case 2 is almost the same as that in Case 1, i.e. for clean interface, as shown in Fig. 6. The high velocity fluid around $\theta = 90$ deg. quickly decelerates due to the Marangoni stress around $\theta = 140$ deg. as shown in Fig. 7 (b). Since the Marangoni stress acts at the interface, the interfacial velocity quickly decreases whereas the effect of the Marangoni stress on the flow away from the interface appears more downstream. Hence, the large velocity gradient and the negative velocity gradient occur around $\theta = 140$ deg. in the outside and inside of the drop, respectively.

4.2 Estimation of Marangoni stress, interfacial tension and surface concentration of surfactant

The difference $\Delta\tau_{r\theta}$ in the viscous stresses between the inside and outside of the drop interface, $\tau_{r\theta,in}$ and $\tau_{r\theta,out}$, reflects the sum of the other forces acting on the interface, i.e., the Marangoni stress and stress due to surface viscosity.

$$\Delta\tau_{r\theta}=\tau_{r\theta,out}-\tau_{r\theta,in} \tag{5}$$

where $\tau_{r\theta}$ is evaluated by

$$\tau_{r\theta} =\mu\left(\frac{\partial v_\theta}{\partial r}\bigg|_{r=R} - \frac{v_{\theta int}}{R}\right) \tag{6}$$

Since the present system is steady and with no interface oscillation, the stress due to surface viscosity could be much smaller than the Marangoni stress. Hence, $\Delta\tau_{r\theta}$ is postulated to depend only on the Marangoni stress in the present system. $\Delta\tau_{r\theta}$ normalized by $\mu_C V_T/R$ is shown in Fig. 8. The normalized $\Delta\tau_{r\theta}$ is almost zero for the clean drop (Case 1), which means there is no jump in the interface shear stress for the clean drop. On the other hand, the normalized $\Delta\tau_{r\theta}$ does not vanish for the fully-contaminated drop (Case 5). Although the normalized $\Delta\tau_{r\theta}$ shows the same trend as the shear stress on a solid sphere indicated by the dashed curve in the figure, it is slightly lower than the shear stress on a sphere. This might be due to non-zero interfacial velocity as shown in Fig. 6 as will be discussed using Eq. (14). In Cases 2, 3 and 4, the normalized $\Delta\tau_{r\theta}$ vanish in the front part of the drop and agree with the fully-contaminated drop in the tail region. This result clearly indicates the

formation of stagnant cap in the rear region of the drop. The region of the stagnant cap increases with C. Non-zero $\Delta\tau_{r\theta}$ in the tail region (θ = 150 – 180 deg.) of the clean drop is due to slight contamination of the liquid. These results clearly indicate that the accurate velocity distribution measured by SFV enables us to evaluate the interface shear stress and the other stresses acting on the interface, which can be utilized for validation of numerical methods for predicting surfactant effects. The Marangoni stress can be estimated by SFV if the surface viscosity is negligible.

Since the Marangoni stress is induced by the gradient of interfacial tension due to accumulation of the surfactant at the interface, we can estimate the local interfacial tension σ by integrating the following equation along the interface by assuming no surface viscosity:

$$\Delta\tau_{r\theta} = \nabla_S \sigma = \frac{1}{R}\frac{\partial \sigma}{\partial \theta} \tag{7}$$

where ∇_S is the surface gradient. The estimated σ is shown in Fig. 9, where σ_T is the interfacial tension at the drop tip. The distributions of $\sigma - \sigma_T$ are smoother than those of $\Delta\tau_{r\theta}$. This is due to the integration which reduces random errors in $\Delta\tau_{r\theta}$. In Case 1, $\sigma - \sigma_T$ is zero, i.e., the interface is clean except in the tail region. In Cases 2 – 4, $\sigma - \sigma_T$ is also zero and constant in the front region, which indicates that σ and Γ are constant in this region. Since the interfacial velocity near the drop nose in Cases 2 – 4 has a gradient in θ direction as shown in Fig. 6, the advection induces non-zero gradient in Γ, in other words in σ, if Γ is not zero. Thus, we can presume that Γ vanishes and the interface is clean at the drop nose, that is, σ_T is equal to the interfacial tension σ_0 ($3.43\text{x}10^{-2}$ N/m) of a clean interface in Cases 2 - 4. To the contrary, $\sigma - \sigma_T$ in the tail region is lower than that in the front region due to the accumulation of surfactant at the interface. The point where $\sigma - \sigma_T$ starts to decrease moves toward the drop tip (θ = 0 deg.) as C increases. The gradient of $\sigma - \sigma_T$ is small in the tail region of the drop and $\sigma - \sigma_T$ at θ = 180 deg. decreases with increasing C.

The relation between σ and surfactant concentration C in the equilibrium state was measured by using a pendant-drop method (Stauffer, 1965) in a quiescent system of the two fluids to evaluate surfactant concentration at the interface from the measured σ. The measured σ decreases with increasing C as shown in Fig. 10

and is well fitted by the following Szyszkowski's equation (Rosen and Kunjappu, 2012):

$$\sigma(\Gamma_{eq}) = \sigma_0 - R_G T \Gamma_{max} \ln\left(1+\frac{C}{a}\right) \tag{8}$$

where R_G is the gas constant, T the temperature, Γ_{eq} the equilibrium surface concentration, Γ_{max} the maximum Γ of monolayer adsorption and a the ratio of rate constants for adsorption and desorption. Γ_{max} and a were evaluated by least square fitting of Eq. (8) to the measured σ, and they were $1.69\text{x}10^{-6}$ mol/m^2 and $1.02\text{x}10^{-3}$ mol/m^3, respectively. σ does not depend on C when $C \geq 2.8\text{x}10^{-1}$ mol/m^3 due to the formation of micelles. Hence, the micelles were not formed in the present experimental range ($C < 1.0\text{x}10^{-1}$ mol/m^3).

Once $\Gamma_{\max}$ and σ_T are known, we can estimate the local surfactant concentration Γ at the interface from the measured $\sigma-\sigma_T$ using the following Frumkin's equation (Frumkin, 1925) by assuming an equilibrium condition.

$$\sigma = \sigma_0 + R_G T \Gamma_{max} \ln\left(1 - \frac{\Gamma}{\Gamma_{max}}\right) \tag{9}$$

Figure 11 shows the estimated local surfactant concentration Γ at the interface for each case. The lines in the figure show Γ_{max} and the equilibrium surfactant concentrations Γ_{eq}. Γ increases with increasing θ due to the adsorption of surfactant to the interface and by the advection of the surfactant on the interface toward the tail, that is, the surfactant adsorbed on the interface flows toward the tail by the interfacial velocity and accumulates in the tail region to form the stagnant cap. In the stagnant cap in the drop tail, $v_{\theta\text{int}}$ vanishes and Γ is almost constant at Γ_{eq} in Cases 2 – 4, i.e., Γ in the tail region reaches the equilibrium state in these conditions. These results imply that (1) the assumption of clean interface at the drop nose is reasonable in these conditions and (2) the adsorption of surfactants is in an equilibrium state and Eq. (9) holds in the present conditions although the applicability of Eq. (9) to a nonequilibrium condition is not guaranteed. Hence, Γ in Case 5 is estimated by assuming that σ at θ = 180 deg. is the same as σ at Γ_{eq}. The tip of the drop in Case 5 is contaminated. The interfacial velocity almost vanishes in Case 5, and therefore, the effect of advection on the surfactant

concentration at the interface becomes very weak. Hence, the difference of Γ between θ = 0 and 180 deg. is small in Case 5, whereas it is large in Cases 2 – 4 due to the advection of Γ. Since the stress due to surface viscosity vanishes for the clean interface and for the stagnant cap region in which the interface is immobile, the effects of the surface viscosity on the estimations occur only in between the clean interface near the drop nose and the stagnant cap near the drop tail. When the surface viscosity is not negligible, the estimated Marangoni stress is larger than the actual value, and therefore, the estimated Γ at the drop tail is higher than the actual values. Since Γ is less than or equal to Γ_{eq} in many cases, the result that Γ at the drop tail is almost the same as Γ_{eq} implies that the stress due to the surface viscosity is negligible in the present conditions. Note that it is not easy to provide all parameters for evaluation of surface viscosity, and therefore, most of numerical simulations of contaminated bubbles or drops do not take into account the surface viscosity. Hence, the present method for estimating Γ based on the assumption of negligible surface viscosity is valuable for validation of numerical simulation even for a system in which the surface viscosity plays some role.

4.3 Discussion on interfacial velocity of fully-contaminated drop

If the Marangoni stress acting on a spherical fluid particle is the same as the viscous stress acting on a solid sphere, we obtain

$$\Delta\tau = \frac{1}{R}\frac{\partial\sigma}{\partial\theta} = -\frac{3}{2}\frac{\mu V_T}{R}sin\theta \tag{10}$$

Integrating Eq. (10) and assuming that Γ at θ = 180 deg. reaches the equilibrium state yield

$$\sigma = \frac{3}{2}\mu V_T(1 + cos\theta) + \sigma\left(\Gamma_{eq}\right) \tag{11}$$

Comparing Eqs. (8), (9) and (11), we obtain

$$\Gamma = \Gamma_{max} - \Gamma_{eq} exp\left\{\frac{3}{2}\frac{\mu V_T}{R_G T\Gamma_{max}}(1 + cos\theta)\right\} \tag{12}$$

Equation (12) is plotted in Fig. 11. Although the trend of the measured Γ in Case 5 agrees with Eq. (12), it is higher than Eq. (12) especially in the front part of the drop. Thus, the gradient of Γ, i.e., the Marangoni stress is smaller than the shear stress at a sphere surface. This explains the non-zero interfacial velocity in Case 5 shown in Fig. 6. Note that the magnitude of the non-zero interfacial velocity is less than a few percentages of the terminal velocity as shown in Fig. 6, so that the effect of the non-zero interfacial velocity on the drop velocity is very small.

The conservation of Γ in the steady state is given by (Levich, 1962, Stone, 1990)

$$\nabla_s \cdot \Gamma \boldsymbol{v}_{int} = \nabla_S \cdot D \nabla_S \Gamma + \dot{S} \tag{13}$$

where $\boldsymbol{v}_{int}$ is the interfacial velocity, D the diffusion coefficient and $\dot{S}$ the molar flux due to adsorption and desorption. If $\boldsymbol{v}_{int}$ vanishes under a fully contaminated condition, the equation (13) reduces to

$$\nabla_S \cdot D \nabla_S \Gamma + \dot{S} = 0 \tag{14}$$

The first term makes Γ constant over the interface and the second term makes Γ approach an equilibrium value. Hence, the equation (14) gives a uniform distribution of Γ. These terms therefore tend to decrease the Marangoni stress. On the other hand, the advection term in Eq. (13) tends to enhance the gradient of Γ and the Marangoni stress. Hence, non-zero $\boldsymbol{v}_{int}$ is necessary even in a fully-contaminated condition and the boundary condition of a fully-contaminated spherical drop is not completely the same as the solid sphere. Note that adsorption of surfactant on an interface decreases C near the interface and the low C region develops toward the drop tail due to advection about the drop. Γ also decreases toward the drop tail due to the decrease in C, and therefore, the Marangoni force acts to increase the interfacial velocity. The present experimental results indicate that the decrease in C in the vicinity of the interface is negligible because Γ at the drop tail reaches Γ_{eq} calculated using the bulk concentration of the surfactant in Fig. 11.

The above results on velocity, interfacial shear stress, Marangoni stress, surface tension and surfactant concentration at the interface of spherical drop can

be utilized for validation of an adsorption-desorption model developed for a quiescent system in numerical simulations of flows with moving interfaces.

4. Conclusion

Spatiotemporal filter velocimetry (SFV) was extended to Lagrangian measurements with boundary-fitted measurement areas for accurate velocity measurements in the vicinity of an interface or boundary. Velocity distributions in the vicinity of single drops of glycerol-water solution falling in stagnant silicone oil were measured by SFV and a refractive index matching method. Experiments were conducted for clean and contaminated conditions to demonstrate the applicability of SFV to the estimation of the Marangoni stress and surfactant concentration at the interface. As a result, we confirmed that SFV accurately measured the velocity distribution in the vicinity of the interface and that the accurate velocity data enabled us to evaluate the interfacial velocity and the interface shear stresses, and to estimate the Marangoni stress, the interfacial tension and the surfactant concentration at the interface with the assumption of negligible surface viscosity. The influence of the surfactant on the velocity distribution was well captured by the SFV measurements. The measured velocity distributions and the measured velocity gradients at the interfaces of the clean and fully-contaminated drops agreed with the Hadamard-Rybczynski and Stokes solutions, respectively. The Marangoni stress was also well estimated from the velocity distribution measured by SFV and it was confirmed that the trend of the Marangoni stress acting on a fully-contaminated spherical drop is the same as that of viscous stress acting on a solid sphere, though its magnitude is slightly lower than that of the viscous stress. The surfactant concentration estimated from the measured velocity distributions gave reasonable values for the various bulk contamination of surfactant.

Acknowledgements

The authors gratefully acknowledge Mr. Kyosuke Kitahata for his effort on the experiments. This work has been supported by the Japan Society for the Promotion of Science (grants-in-aid for scientific research (C) No. 16K06083 and (B) No. 25289033).

Nomenclature

a:	ratio of rate constants for adsorption and desorption	[mol/m^3]
C:	concentration of surfactant	[mol/m^3]
D:	diffusion coefficient	[m^2/s]
d:	drop diameter	[m]
F_{SF}:	spatiotemporal filter function	
I:	intensity	
I_{SF}:	integrated intensity	
L:	cycle of spatiotemporal filter function	[m]
M:	window function	
R:	drop radii	[m]
R_G:	gas constant	[J/K/mol]
r:	coordinate in radial direction	[m]
$\dot{S}$:	molar flux due to adsorption and desorption	[mol/m^2/s]
T:	temperature	[K]
t:	time	[s]
V_T:	terminal velocity	[m/s]
v:	velocity	[m/s]
x:	coordinate in horizontal direction	[m]
y:	coordinate in vertical direction	[m]
x_c, y_c:	center position of interrogation area in x and y directions	[m]
$\Delta\tau$:	Marangoni stress	[Pa]
Δx, Δy:	size of interrogation area in x and y directions	[m]
Γ:	surfactant concentration at interfacial	[mol/m^2]
κ:	viscosity ratio	
μ:	viscosity	[Pa s]
θ:	coordinate in tangential direction	[deg.]
ρ:	density	[kg/m^3]
σ:	interfacial tension	[N/m]
τ:	interfacial shear stress	[Pa]
ξ, η:	curvilinear coordinates	[m]

Subscript

0: clean system

C: continuous phase

D: drop

eq: equilibrium

in: inside of drop

int: interface

max: maximum

out: outside of drop

S: surface

T: drop tip

x: *x* component

y: *y* component

θ: θ component

θ*int*: θ component at interface

Appendix

Velocity measurement using rectangular measurement areas was carried out to examine advantages of the boundary-fitted measurement areas in velocity and velocity gradient measurements. The image processing procedure is shown in Fig. A1. Since the measured velocity in the measurement area containing an interface is an averaged value of the velocities in both phases, we introduced an image window to discriminate particles in one phase from those in the other phase. That is, the original image was binarized with a threshold level which was determined as an intermediate level between the intensity of fluorescence in the drop and that of background in the outside. The binarized image contained tracer particles in the outside region, and the particles were removed by using a morphological filter to obtain the image window for extracting the inside particles. The image window for the outside particles was obtained by inverting the image window for the inside particles. These windows indicate a phase distribution and we call them as the phase indicator window, MP. The original images were masked by a rectangular mask moving with the drop (Lagrangian mask: ML) and one of the phase indicator windows to obtain time-series particle images in the inside or outside of the drop. Thus, M in Eq. (2) is the product of MP and ML. Each set of time-series images of

particles was analyzed by SFV to obtain velocity distributions in the inside and outside of the drop. Hence, the effective measurement area containing an interface is not rectangle but non-rectangular as shown in Fig. A2. The definition point of the measured vector was set at the center of the filtered measurement area, thus, velocities of both phases were measured in a rectangular measurement area containing an interface.

The interfacial velocities $v_{\theta int}$ measured using the rectangular measurement areas in Cases 1 and 5 was plotted in Fig. A3 together with those using the boundary-fitted measurement areas. The curves indicate the theories given by Eqs. (3) and (4). Although there is small difference between the velocities measured by both methods in Case 5 in which $v_{\theta int}$ is nearly zero, the difference between the theoretical and measured $v_{\theta int}$ in the case using the rectangular area is larger than that in the case using the boundary-fitted area. Figure A4 shows the normalized Marangoni stress $\Delta\tau_{r\theta}/(\mu_C V_T/R)$ which was estimated from the velocity distributions measured by the two methods. The difference between the theories and the data measured using the rectangular area is larger than those using the boundary-fitted area not only in Case 1 but also in Case 5. This is due to not only measurement error but also error in interpolation of rectangularly arranged data to obtain the radial gradient of the tangential velocity. These results clearly indicate that the boundary-fitted measurement area improves accuracy in SFV measurement of flow containing a curved interface or boundary.

References

Bain, C.D., 1998, Studies of Adsorption at Interface by Optical Techniques: Ellipsometry, Second Harmonic Generation and Sum-Frequency Generation, Current Opinion in Colloid & Interface Science, Vol. 3, Issue 3, 287 – 292.

Borwankar, R.P. and Wasan, D.T., 1983, The kinetics of adsorption of surface active agent at gas-liquid surfaces, Chemical Engineering Science, Vol. 38, No. 10, pp. 1637 – 1649.

Bleys, G. and Joos, P., 1985, Adsorption kinetics of bolaform surfactants at the air/water interface, Journal of Physical Chemistry, Vol. 89, pp. 1027 – 1032.

Bull JL, Nelson LK, Walsh JT, Jr., Glucksberg MR, Schürch SS, Grotberg JB., 1999, Surfactant-Spreading and Surface-Compression Disturbance on a Thin Viscous Film. ASME. *J Biomech Eng.*, Vol. 121, Issue 1, 89-98.

Clift, R, Grace, J.R., Weber, M.E., 1978, Bubbles, Drops and Particles, Academic Press.

Cuenot, B., Magnaudet, J. and Spennato, B., 1997, The effect of slightly soluble surfactants on the flow around a spherical bubble, Journal of Fluid Mechanics, Vol. 339, pp. 25 – 53.

Dixon, J.K, Weith, A.J., Argyle, A.A. and Salley, D.J., 1949, Measurement of the Adsorption of Surface-Active Agent at a Solution-Air Interface by a Radiotracer Method, Nature, 163, 845.

Fallest, D.W., Lichtenberger, A.M., Fox, C.J. and Daniels, K.E., 2010, Fluorescent Visualization of a Spreading Surfactant, New Jouranl of Physics, Vol. 12, 073029.

Frumkin, A., 1925, Electrocapillary Curve of Higher Aliphatic Acids and the State Equation of the Surface Layer, Z Phys. Chem., Vol. 116, p. 466.

Hayashi, K. and Tomiyama, A., 2012, Effects of surfactant on terminal velocity of a Taylor bubble in a vertical pipe, International Journal of Multiphase Flow, Vol. 39, pp. 78 – 87.

Hosokawa, S. and Tomiyama, A., 2012, Spatial Filter Velocimetry based on Time-Series Particle Images, *Experiments in Fluids*, Vol. 52, pp. 1361 – 1372.

Hosokawa, S., Matsumoto, T. and Tomiyama, A., 2013, Measurement of Bubble Velocity using Spatial Filter Velocimetry, *Experiments in Fluids*, Vol. 54, Article: 1538.

Hutchison, J., Klenerman, D., Manning-Benson, S. and Bain, C., 1999, Measurement of the Adsorption Kinetics of a Cationic Surfactant in a Liquid Jet by Ellipsometry, Langmuir, Vol. 15, 7530 – 7533.

Levich, 1962, Physicochemical Hydrodynamics, Prentice Hall, 1962.

Manning-Benson, S., Bain, C.D. and Darton, R.C., 1997, Measurement of Dynamic Interfacial Properties in an Overflowing Cylinder by Ellipsometry, Journal of Colloid and Interface Science, Vol. 189, 109 – 116.

Manning-Benson, S., Parker, S.R.W. and Bain, C.D., 1998, Measurement of the Dynamic Surface Excess in an Overflowing Cylinder by Neutron Reflection, Langmuir, 14, 990 – 996.

Ninomiya, N. and Yasuda, K., 2006, Visualization and PIV Measurement of the Flow around and inside of a Falling Droplet, *Journal of Visualization*, Vol. 9, pp. 257 – 264.

Oguma, Y. and Fujisawa, N., 2007, Near-wall velocity measurement over an airfoil by PIV, *Journal of Visualization*, Vol. 10, No. 2, pp. 157–158.

Rosen, M.J. and Kunjappu, J.T., 2012, Surfactants and Interfacial Phenomena, Wiley.

Stauffer, C.E., 1965, The Measurement of Surface Tension by the Pendant Drop Technique, Journal of Physical Chemistry, Vol. 69 (6), pp. 1933 – 1938.

Stone, H.A., 1990, A simple derivation of the time-dependent convective-diffusion equation for surfactant transport along a deforming interface, Physics of Fluids, A 2(1), 111 – 112.

Strickland, S.L., Shearer, M. and Daniels, K.E., 2015, Spatiotemporal measurement of surfactant distribution on gravity-capillary waves, Journal of Fluid Mechnics, Vol. 777, 523 – 543.

Shen, Y.R., 1989, Surface Properties probed by Second-Harmonics and Sum-Frequency Generation, Nature, 337, 519 – 525.

Tajima, K., Muramatsu, M. and Sasaki, T., 1970, Radiotracer Studies on Adsorption of Surface Active Substance at Aqueous Surface. I. Accurate Measurement of Adsorption of Tritiated Sodium Dodecylsulfate, Bulletin of The Chemical Society of Japan, Vol. 43, 1991 – 1998.

Takiue, T., Kawagoe, Y., Muroi, S., Murakami, R., Ikeda, N. and Aratono, M., 2003, Surface Density Measurement of the Bromide Ion by the Total-Reflection X-ray Absorption Fine

Structure Technique at the Air/Aqueous Dodecyltrimethylammonium Bromide Solution Interface, Langmuir, 19, 10803 – 10807.

Vogel, M.J., Hisa, A.H., Kelley, J.S. and Korenowski, G.M., 2001, Simultaneous Measurement of Free-Surface Velocity and Surfactant Concentration via a Common Laser Probe, Review of Scientific Instruments, Vol. 72, Number 2, 1502 – 1509.

Figure captions

Fig. 1 Principle of spatiotemporal filter velocimetry.

Fig. 2 SFV for boundary fitted interrogation area.

Fig. 3 Experimental setup.

Fig. 4 Effect of contamination level on velocity distribution about a falling drop. ((a) Case1: C = 0.0 mol/m^3 (0.0% CMC: clean), (b) Case 2, C = 2.0 x 10^{-3} mol/m^3 (0.7% CMC), (c) Case 3, C = 5.0 x 10^{-3} mol/m^3 (1.8% CMC), (d) Case 4, C = 1.0 x 10^{-2} mol/m^3 (3.6% CMC), (b) Case 5, C = 1.0 x 10^{-1} mol/m^3 (35.7% CMC: fully-contaminated))

Fig. 5 Tangential velocity distribution in inside and outside of a drop.

Fig. 6 Tangential velocity distribution at drop interface. (The solid and dashed curves indicate the Hadamard-Rybczynski and Stokes solutions, respectively.)

Fig. 7 Velocity gradients at interface.

(a) Distributions of velocity gradients at interface. (The solid and dashed curves indicate the Hadamard-Rybczynski and Stokes solutions, respectively.)

(b) Schematic of velocity distribution modulated by the Marangoni stress

Fig. 8 Difference between viscous shear stresses between the inside and outside of the drop interface. (The solid and dashed curves indicate the Hadamard-Rybczynski and Stokes solutions, respectively.)

Fig. 9 Distribution of estimated local interfacial tension.

Fig. 10 Effect of C on σ.

Fig. 11 Distribution of estimated surfactant concentration at interface.

Fig. A1 Image processing procedure.

Fig. A2 Definition points of velocities in a rectangular area containing an interface.

Fig. A3 Comparison of tangential velocity distributions measured by SFVs using rectangular and boundary-fitted measurement areas.

Fig. A4 Comparison of the Marangoni stress estimated from velocity distributions measured by SFVs using rectangular and boundary-fitted measurement areas.

Table1 Experimental conditions

Table1 Experimental conditions

	Case 1	Case 2	Case 3	Case 4	Case 5
Concentration of Triton X-100:C [x10^{-2} mol/m^3]	0 (0% CMC)	0.2 (0.7% CMC)	0.5 (1.8% CMC)	1.0 (3.6% CMC)	10.0 (35.7% CMC)
Drop diameter: d [mm]	8.3	8.3	8.3	8.3	8.3
Terminal velocity: V_T [x 10^{-2} m/s]	2.75	2.54	2.15	1.95	1.86
Reynolds number: Re	0.73	0.69	0.59	0.52	0.50

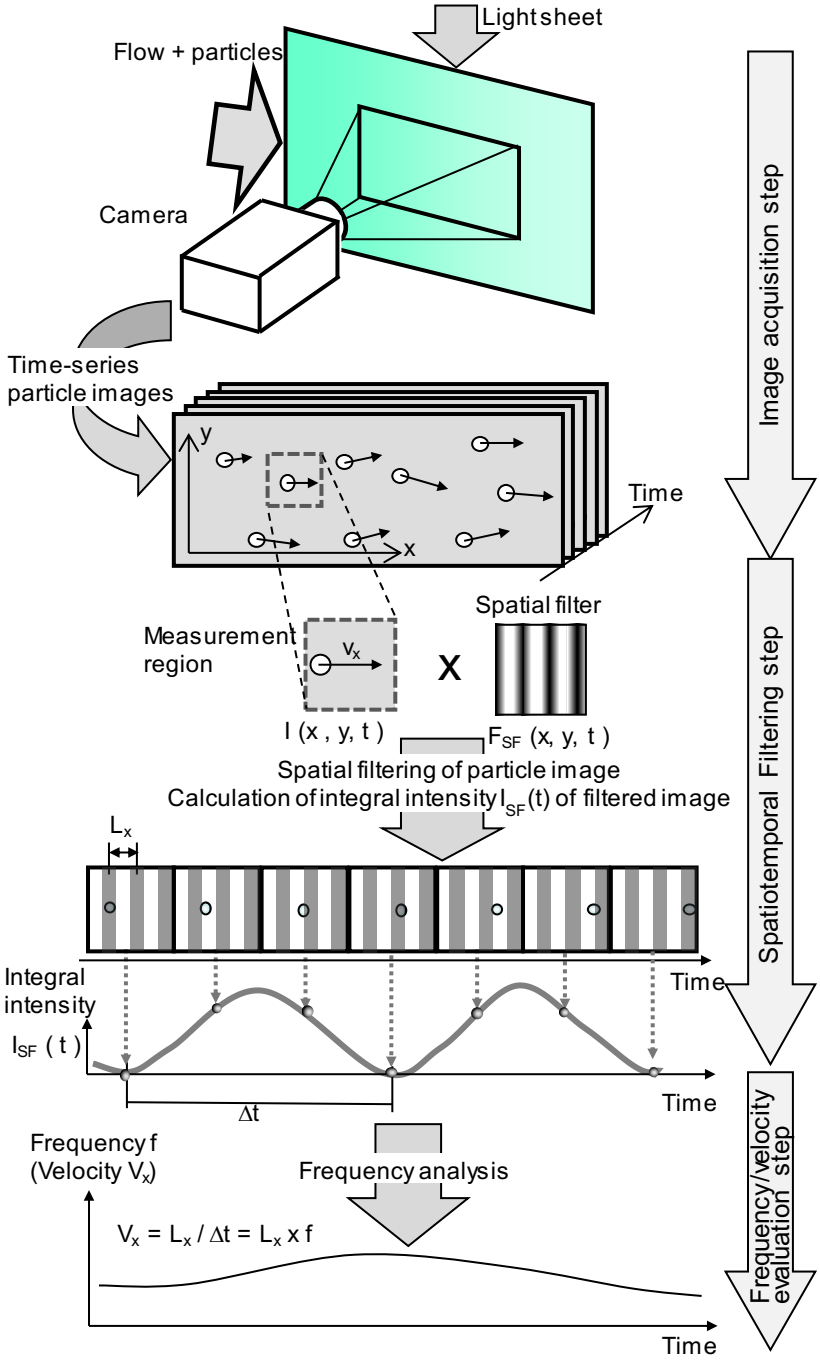

Fig. 1 Principle of spatiotemporal filter velocimetry.

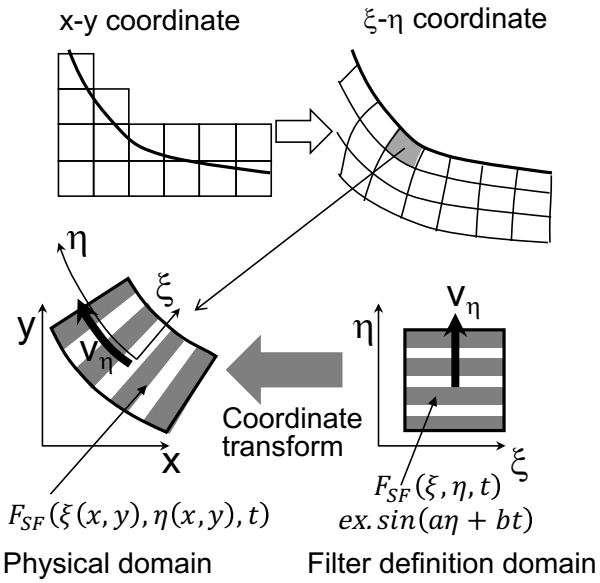

Fig. 2 SFV for boundary fitted interrogation area.

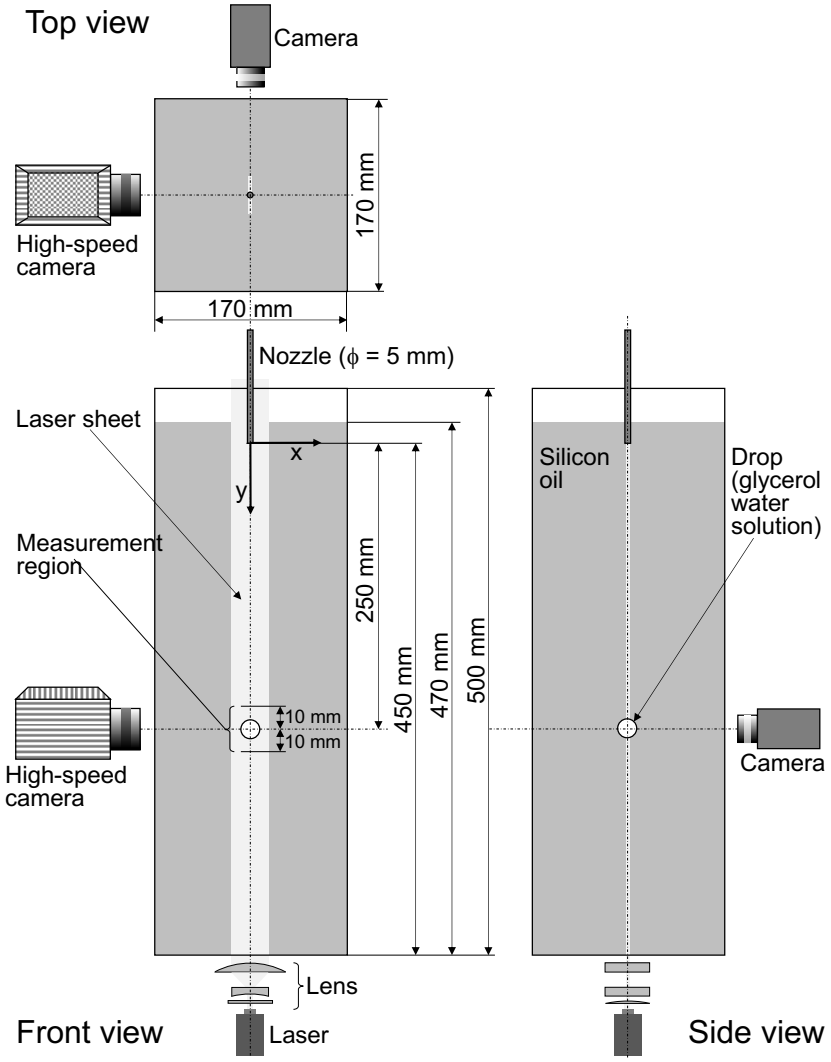

Fig. 3 Experimental setup.

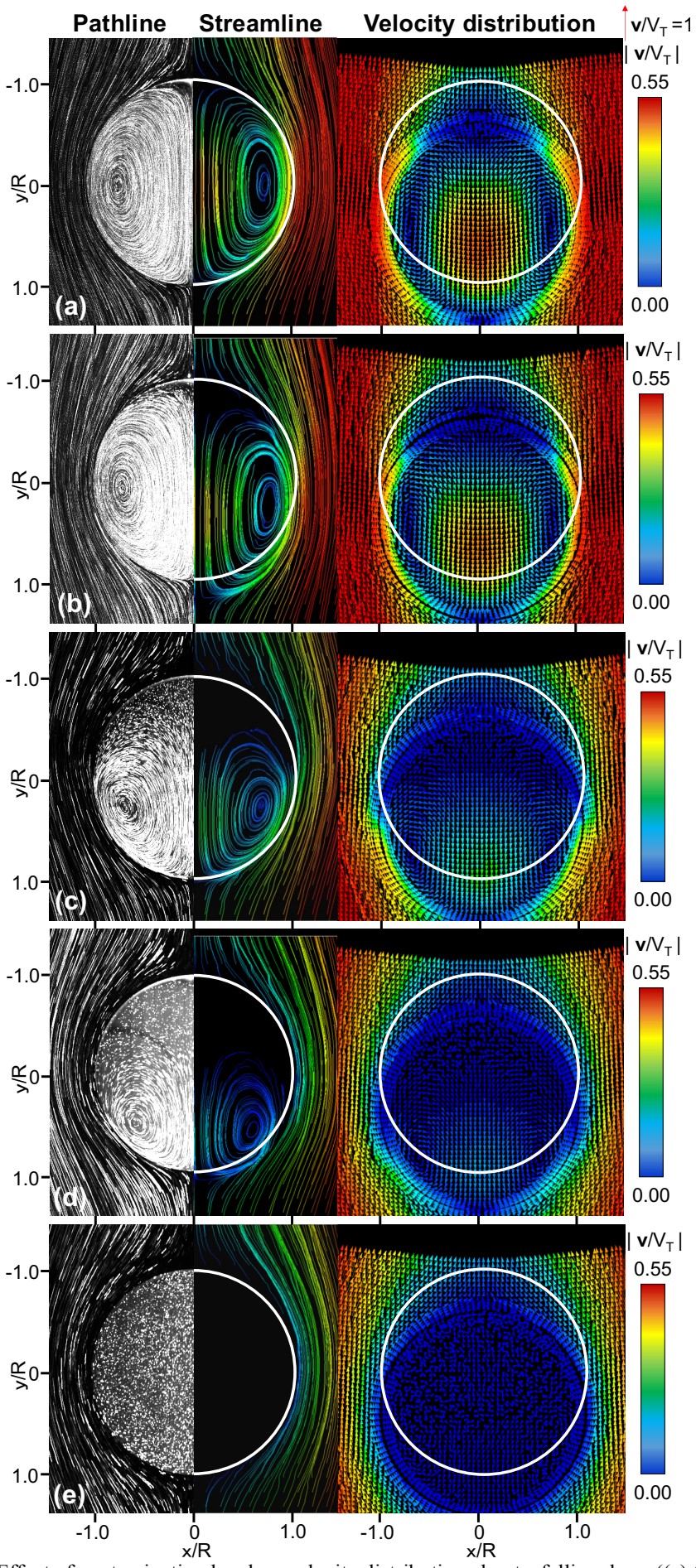

Fig. 4 Effect of contamination level on velocity distribution about a falling drop. ((a) Case1: C = 0.0 mol/m^3 (0.0% CMC: clean), (b) Case 2, C = 2.0 x 10^{-3} mol/m^3 (0.7% CMC), (c) Case 3, C = 5.0 x 10^{-3} mol/m^3 (1.8% CMC), (d) Case 4, C = 1.0 x 10^{-2} mol/m^3 (3.6% CMC), (b) Case 5, C = 1.0 x 10^{-1} mol/m^3 (35.7% CMC: fully-contaminated))

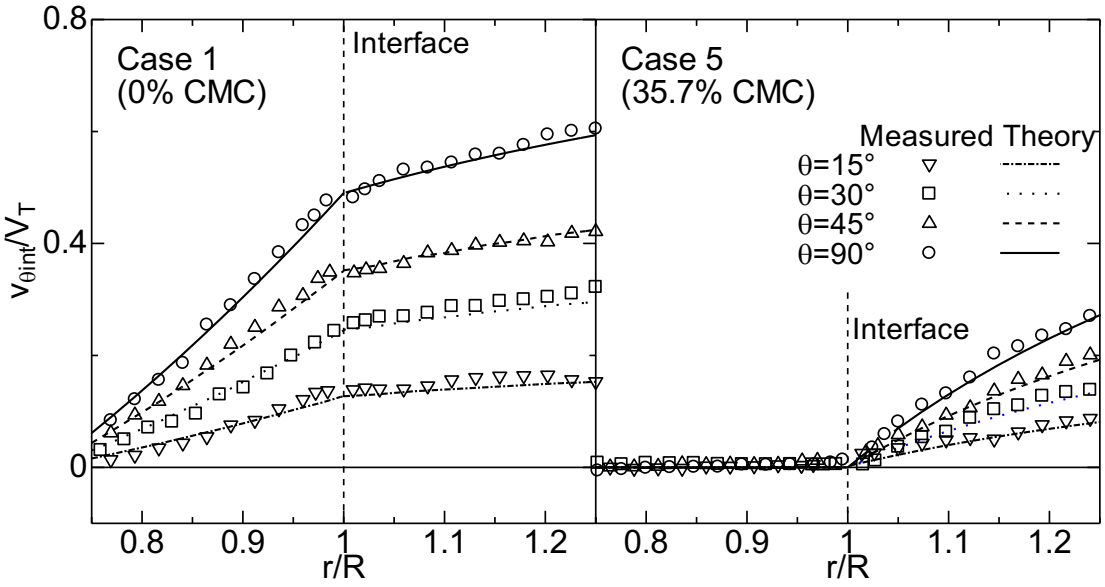

(a) Clean drop (b) Contaminated drop

Fig. 5 Tangential velocity distribution in inside and outside of a drop.

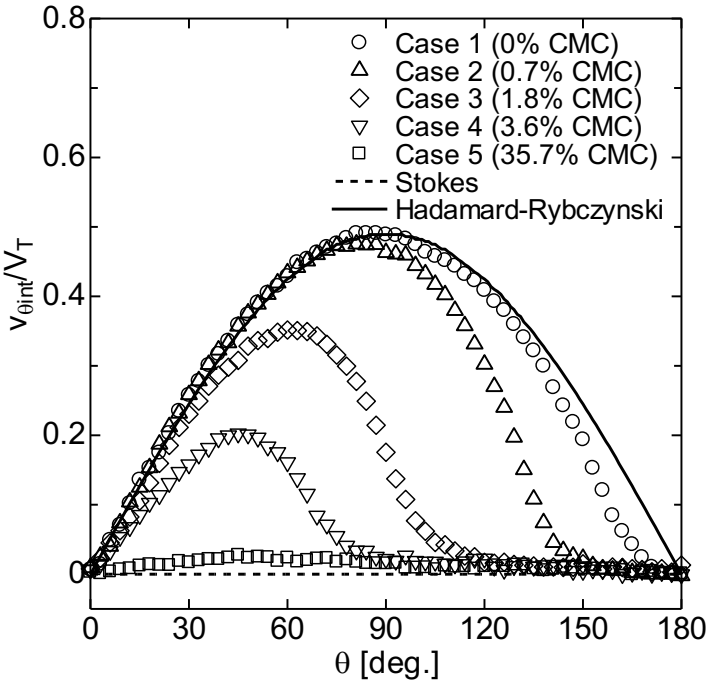

Fig. 6 Tangential velocity distribution at drop interface. (The solid and dashed curves indicate the Hadamard-Rybczynski and Stokes solutions, respectively.)

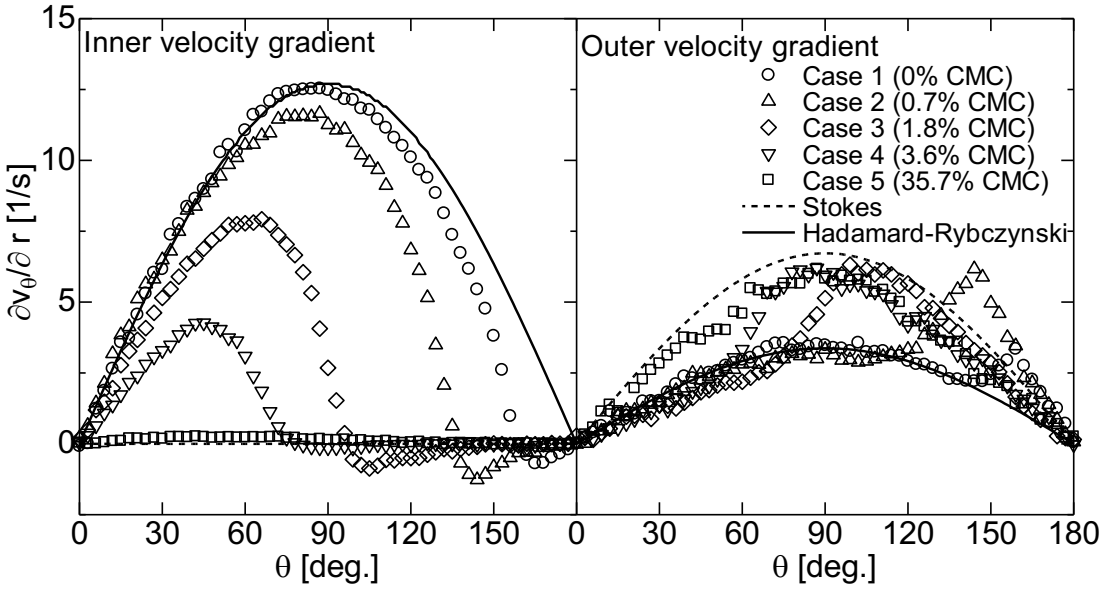

(a) Distributions of velocity gradients at interface. (The solid and dashed curves indicate the Hadamard-Rybczynski and Stokes solutions, respectively.)

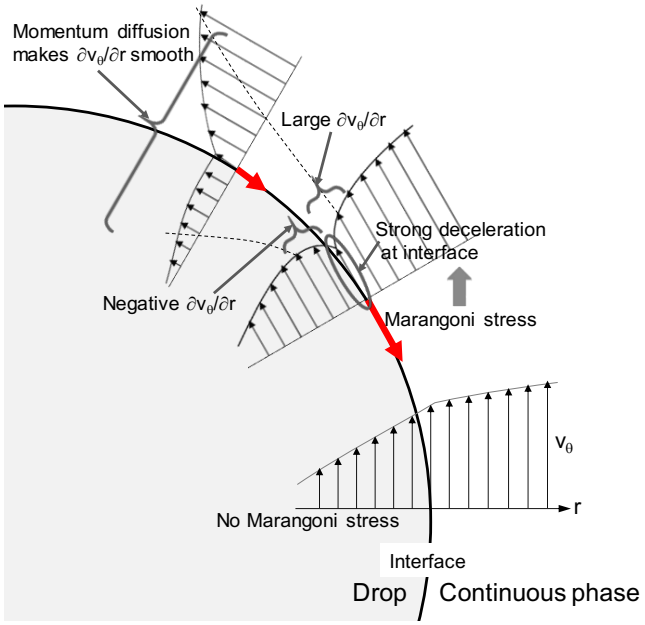

(b) Schematic of velocity distribution modulated by the Marangoni stress

Fig. 7 Velocity gradients at interface.

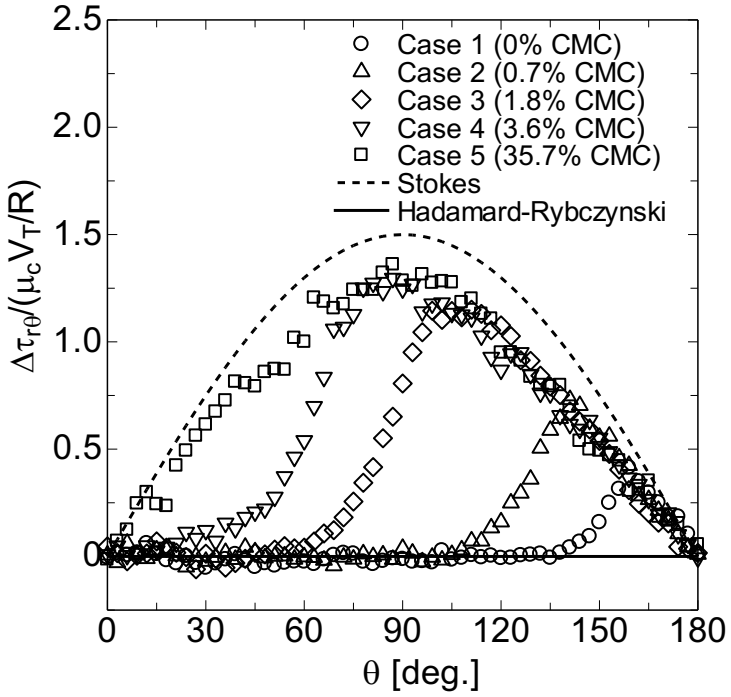

Fig. 8 Difference between viscous shear stresses between the inside and outside of the drop interface. (The solid and dashed curves indicate the Hadamard-Rybczynski and Stokes solutions, respectively.)

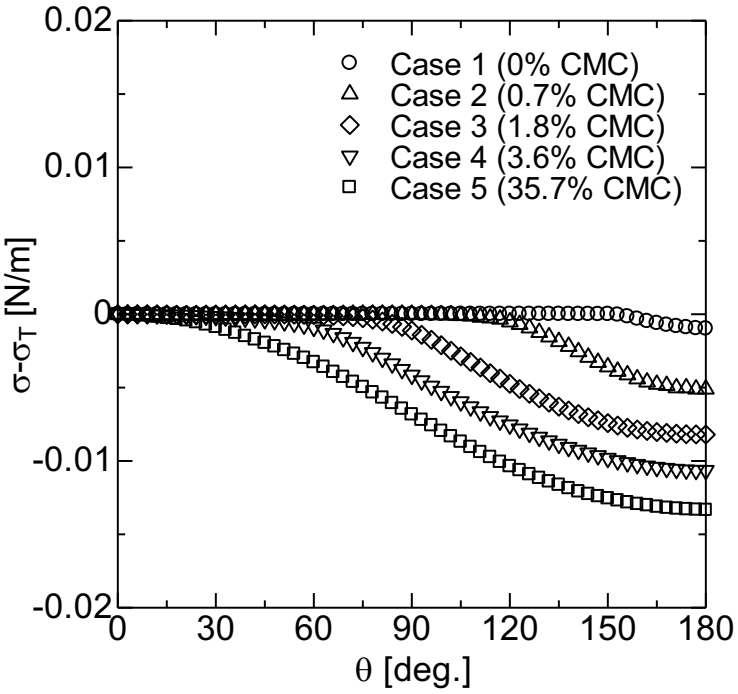

Fig. 9 Distribution of estimated local interfacial tension.

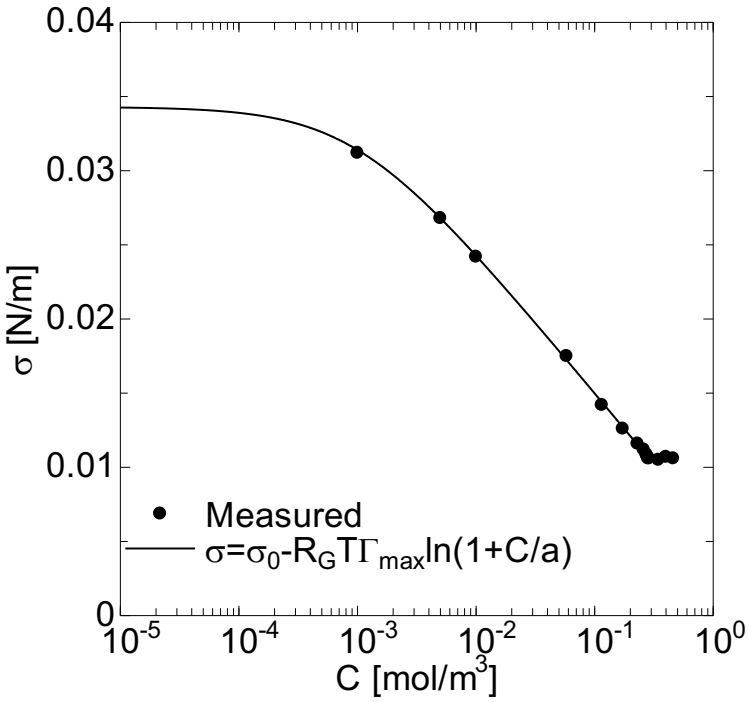

Fig. 10 Effect of C on σ.

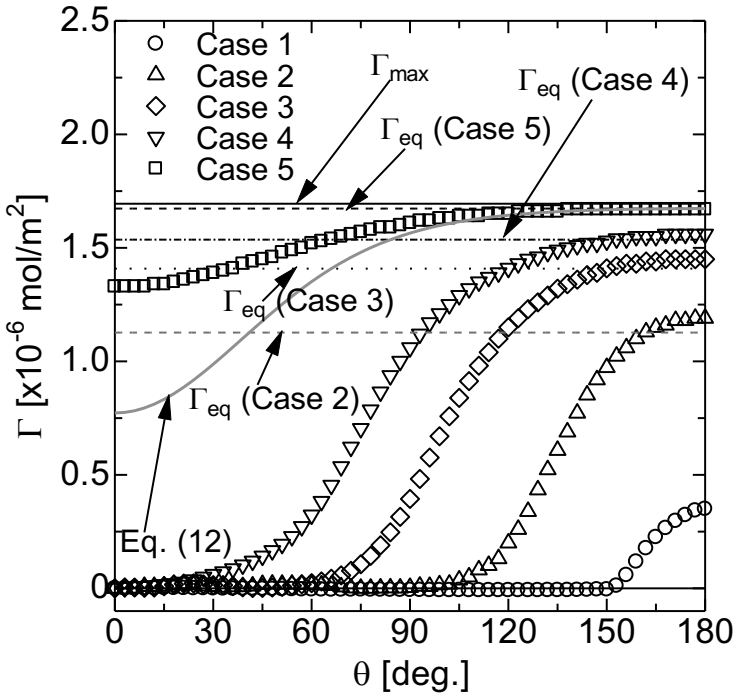

Fig. 11 Distribution of estimated surfactant concentration at interface.

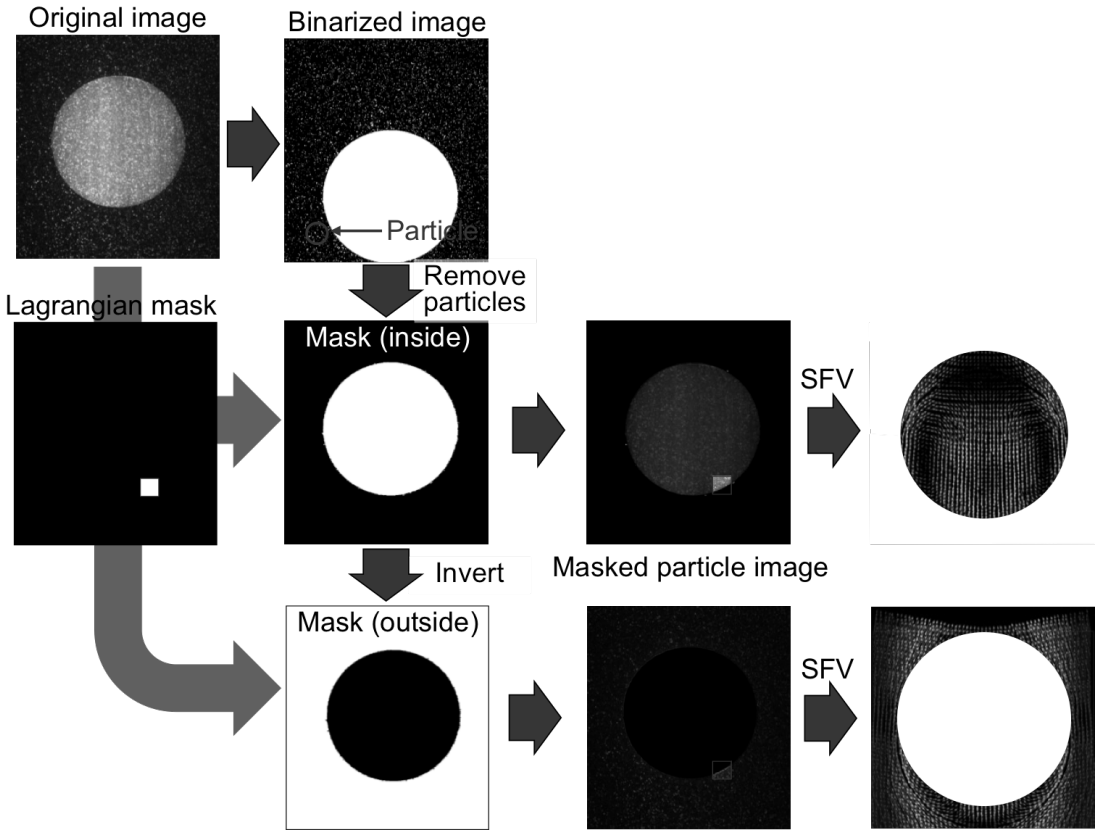

Fig. A1 Image processing procedure.

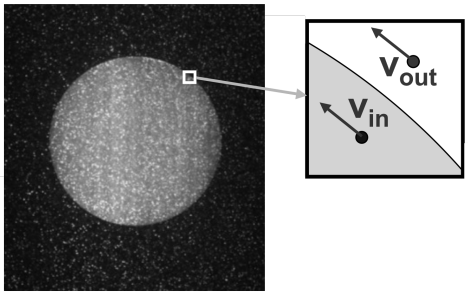

Fig. A2 Definition points of velocities in a rectangular area containing an interface.

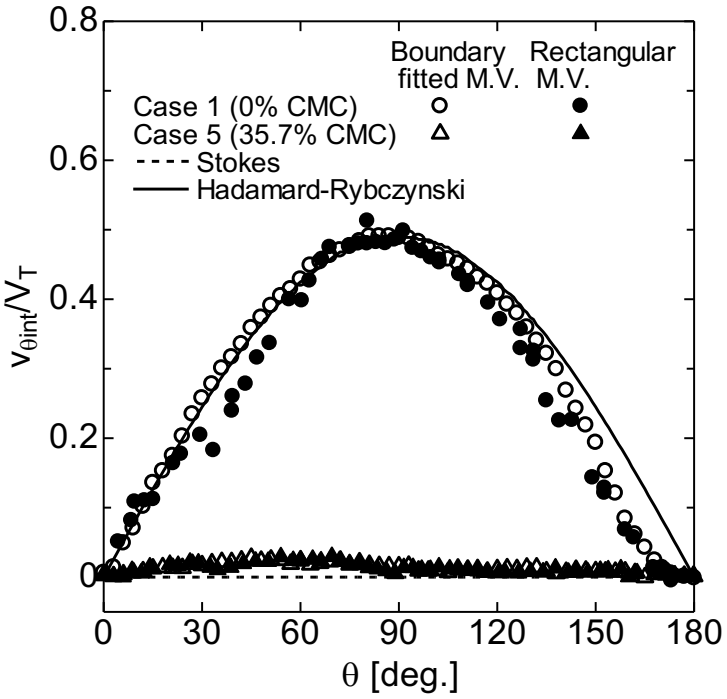

Fig. A3 Comparison of tangential velocity distributions measured by SFVs using rectangular and boundary-fitted measurement areas.

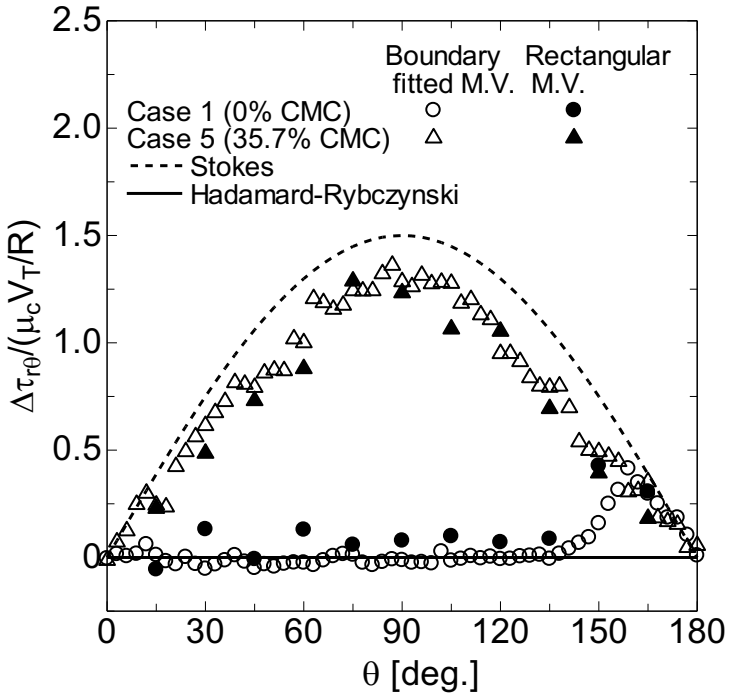

Fig. A4 Comparison of the Marangoni stress estimated from velocity distributions measured by SFVs using rectangular and boundary-fitted measurement areas.